Supplementary Material

In Situ MOF-templating of Rh Nanocatalysts under Reducing Conditions

Renata Lippi,[A,B,E] Campbell J. Coghlan,[A] Shaun C. Howard,[B] Christopher D. Easton,[B] Qinfen Gu,[C] Jim Patel,[D] Christopher J. Sumby,[A] Danielle F. Kennedy,[B] and Christian J. Doonan[A]

[A]Centre for Advanced Nanomaterials, Department of Chemistry, The University of Adelaide, Adelaide, SA 5005, Australia.
[B]CSIRO Manufacturing, Clayton, Vic. 3168, Australia.
[C]Australian Synchrotron (ANSTO), Clayton, Vic. 3168, Australia.
[D]CSIRO Energy, Clayton, Vic. 3168, Australia.
[E]Corresponding author. Email: renata.lippi@csiro.au

Contents

A. Experimental methods

A.1 Materials

All materials were used as provided by the manufacturer, unless stated otherwise. Di-μ-chloro-tetracarbonyldirhodium(I) ($[Rh(CO)_2Cl]_2$) 97% Sigma Aldrich (Australia), sodium tetrafluoroborate ($NaBF_4$) 98% Sigma Aldrich (Australia), Manganese(II) chloride ($MnCl_2$) 98% Sigma Aldrich (Australia), N-N-dimethylformamide (DMF) 99.8% Merck Pty. Ltd. (Australia), anhydrous acetonitrile (CH_3CN) max. 0.005% H_2O Merck Pty. Ltd. (Australia), Silicon Carbide (SiC) 99% 300-355 μm Beijing HWRK Chem Co., Ltd. (China). Water was deionized by reverse osmosis. All gases used were supplied by Coregas (Australia) including custom made mixtures: nitrogen (N4); Argon (N5); Helium (N5); Hydrogen (N5); 25% carbon dioxide with hydrogen balance; and 2.52% ethane, 2.82% ethene, 2.53% acetylene, 2.44% methane, 2.48% carbon dioxide, 2.53% carbon monoxide, 2.51% hydrogen with argon balance, 5% hydrogen with argon balance.

A.2 Thermogravimetric analysis (TGA)

Samples were loaded into Al_2O_3 crucibles and evaluated using a Mettler Toledo TGA 2. The samples were heated to 800 °C at 10 °C/min under N_2 purge gas at 30 mL/min. The sample was allowed to equilibrate at 25 °C in N_2 before the analysis, this section is not shown in the thermogram.
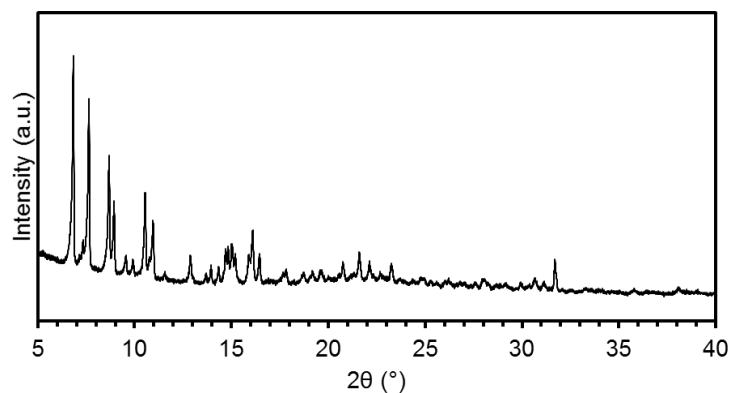
B. Supporting results

B.1 MOF Characterization
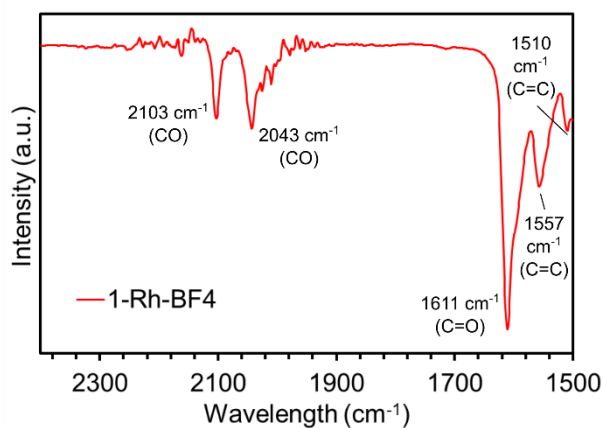

Figure S1: PXRD of 1-Rh-BF$_4$ with Cu radiation.

Figure S2: IR spectrum of **1**-Rh-BF$_4$. The displacement of the counter-ion [Rh(CO)$_2$Cl$_2$]$^-$ by [BF$_4$]$^-$ in the MOF is confirmed by the presence of only two major peaks in the region from 2200 and 1900 cm^{-1}. In contrast, the presence of the counter-ion [Rh(CO)$_2$Cl$_2$]$^-$ in **1**-Rh$_2$ contributes to a total of five different absorption wavelengths in this region.[1]
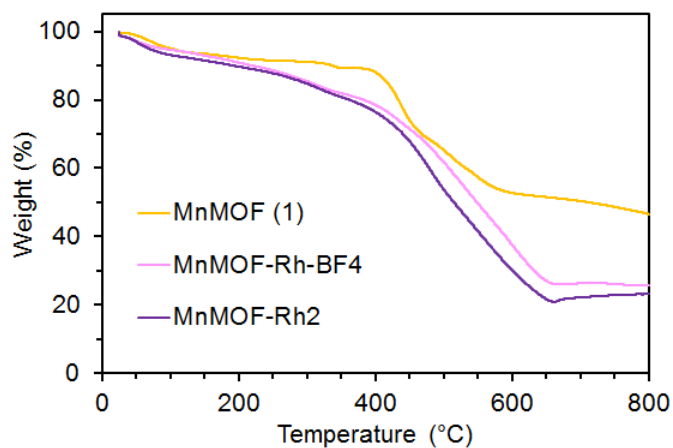
Figure S3: Thermogravimetric analysis of **1**, **1**-Rh-BF$_4$ and **1**-Rh$_2$ in N$_2$ (40 mL/min). Both MnMOF (**1**) and its post synthetically metalated versions display high thermal stability up to 400 °C. From 100 to 400 °C MnMOF (**1**) loses 7 wt% and both **1**-Rh-BF$_4$ and **1**-Rh$_2$ lose 17 wt%.
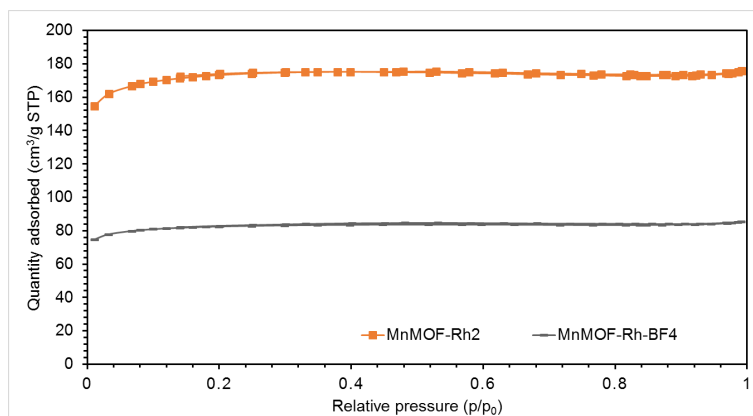

Figure S4: N$_2$ adsorption isotherm for **1**-Rh-BF$_4$ and **1**-Rh$_2$.

Table S1. BET surface area results. The low surface area for **1**-Rh-BF$_4$ is explained by the presence of NaCl crystals (by-product of the counter-ion exchange) likely blocking some of the pores.

Sample	BET surface area (m²/g)
1-Rh$_2$	581.5
1-Rh-BF$_4$	276.6

B.2 Catalysis results
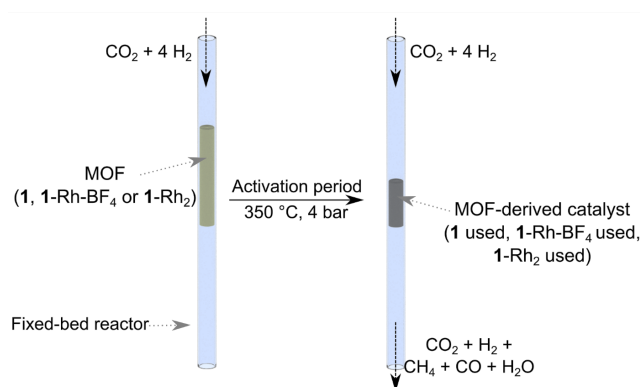
Figure S5: Scheme of *in situ* catalyst activation. Fixed-bed microreactor loaded with MOF (left) and MOF-templated catalyst (right) activated under reaction conditions, i.e. in situ.

Figure S6: Comparison of average CH$_4$ production for **1**-Rh-BF$_4$ and **1**-Rh$_2$. A lower production rate of CH$_4$ is observed for the sample where the counter-ion [Rh(CO)Cl$_2$]$^-$ has been displaced. In condition D **1**-Rh$_2$ produces approximately double the amount of CH$_4$ than **1**-Rh-BF$_4$.

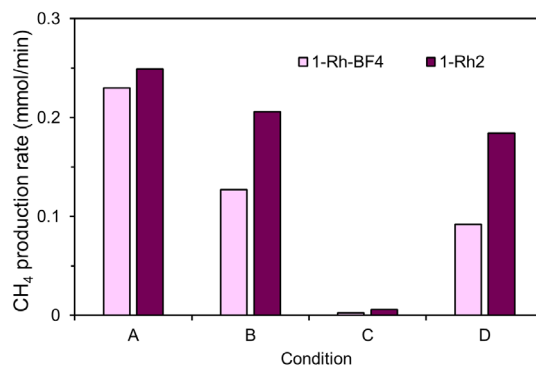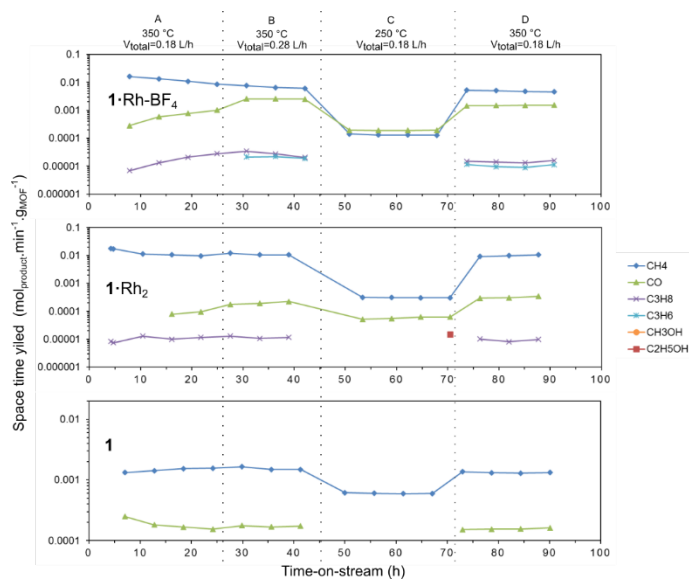**Figure S7:** Space-time yield in logarithmic scale for the different precatalysts tested in parallel for CO_2 hydrogenation (Figure 2). Scale used to display with clarity the presence of products in trace amounts.
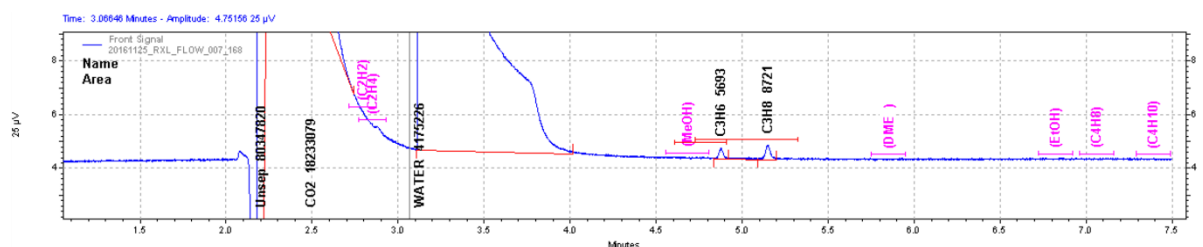
Figure S8: Example of chromatogram of effluent gas from **1**-Rh-BF$_4$-used. The authors note that the presence of C2 products could not be evaluated due to the proximity of their retention time with CO_2 and water, which were present in high amounts in the gas effluent. However, the presence of C3 is clearly visible.

B.3   XRD
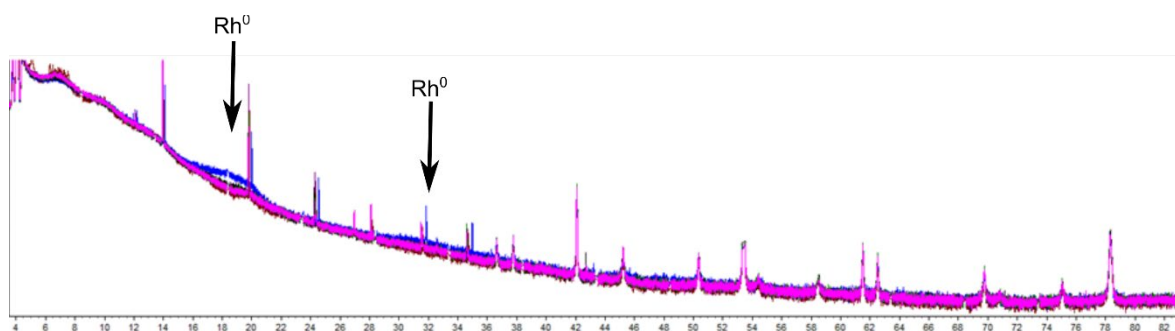
Figure S9: Comparison of XRD patterns from datasets 18, 30 and 50 of **1**·Rh-BF$_4$ in situ XRD experiment (Figure 5). Intensity increase is observed around 19° and 32°, where Rh^0 reflections are expected, indicating the formation of Rh^0 nanoparticles. The shift of other peaks is due to thermal expansion as temperature varied in the course of this experiment.

B.4   TEM nanoparticle sizing
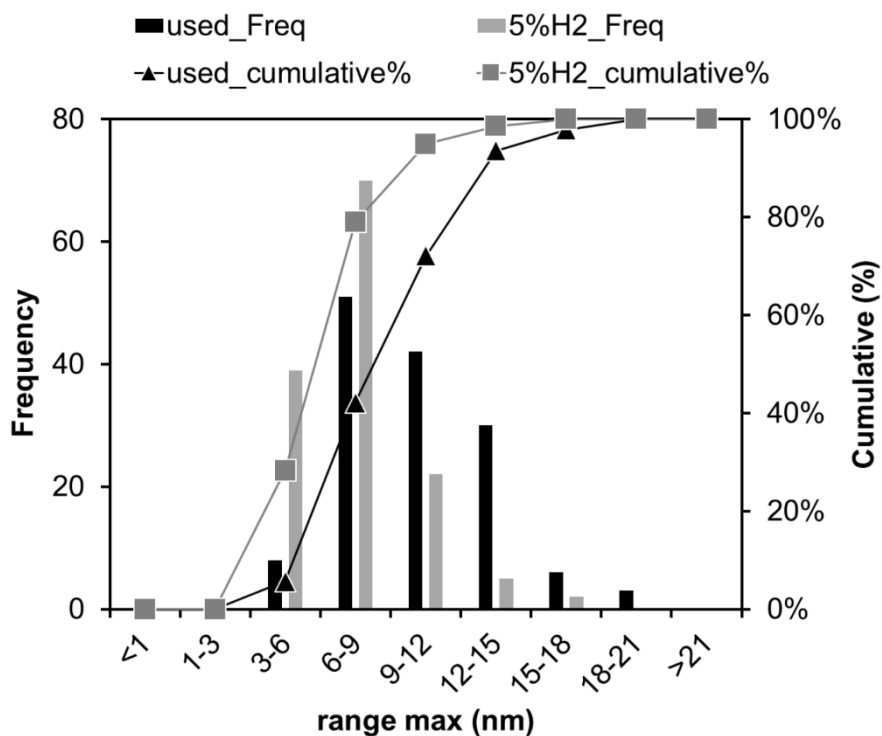
Figure S10: Histogram of Rh^0 nanoparticles size distribution **1**·Rh-BF$_4$-5%H$_2$ and **1**·Rh-BF$_4$-used.

B.5 EDS mapping

Figure S11: SEM and EDS element maps for **1**-Rh-BF$_4$ and **1** after catalysis testing (used).

Figure S12: SEM and EDS element maps for **1**-Rh-BF$_4$ and **1** after reduction in 5%H$_2$.

B.6 X-ray photoelectron spectroscopy

B.7 Elemental quantification

Table S2: XPS elemental composition.

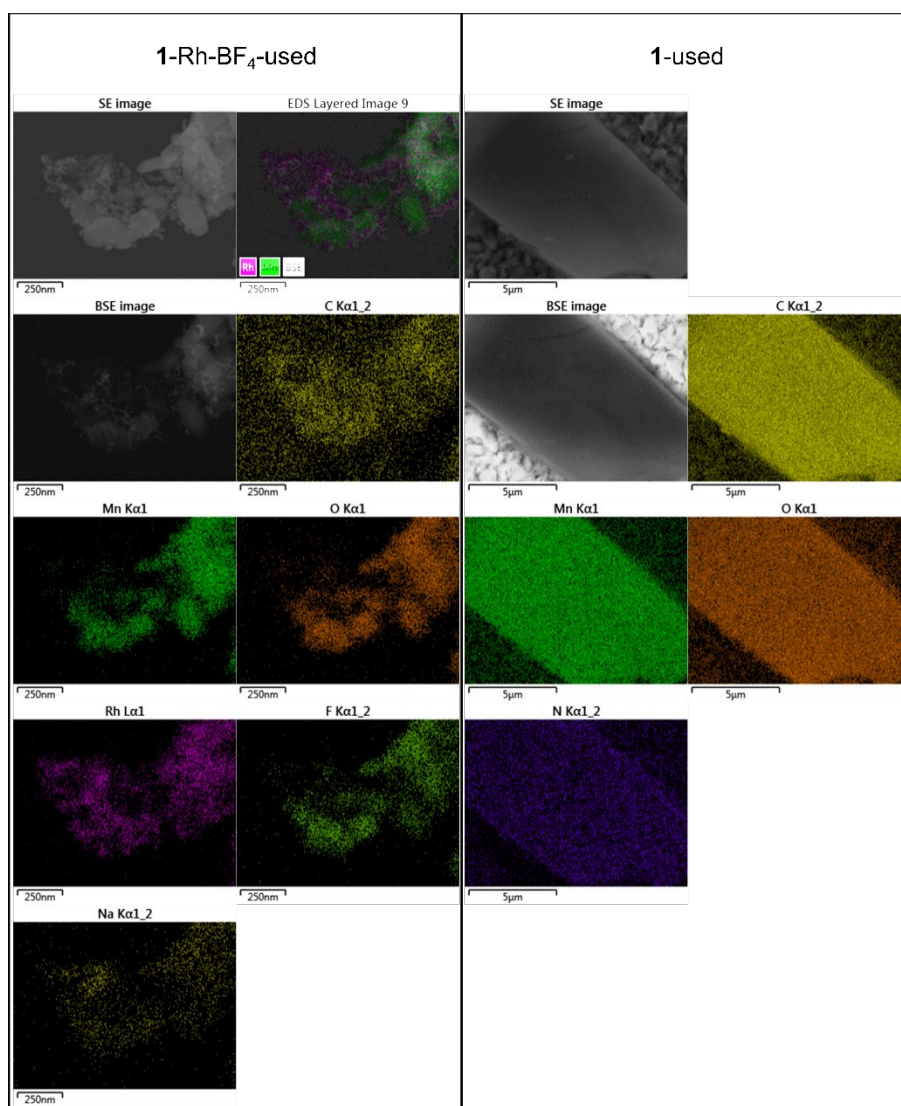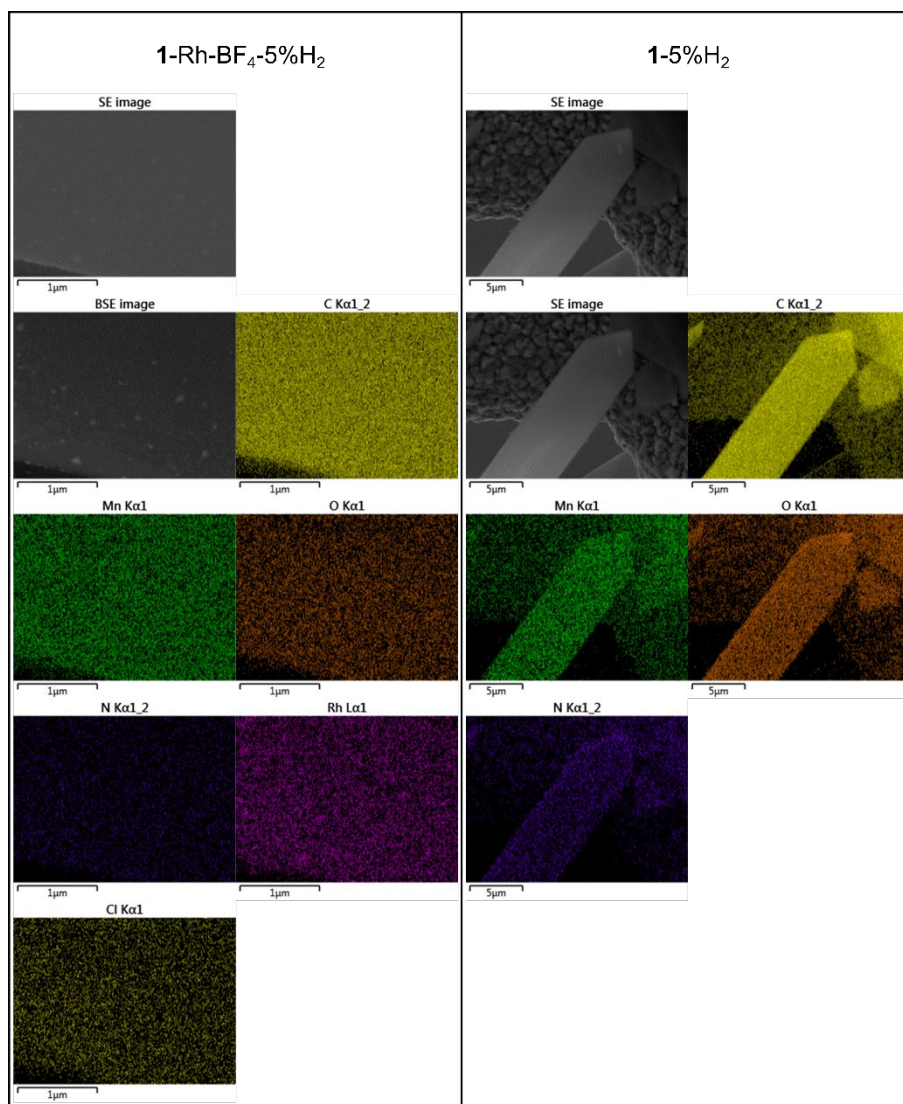| Elements	Atomic composition (%) ± standard deviation (n = 2)					
	MnMOF (1)	1-5%H2	1 used (normalized)	1-Rh-BF4	1-Rh-BF4-5%H2	1-Rh-BF4 used
C	74.83 ± 0.01	74.72 ± 0.29	73.0	72.1 ± 0.21	73.14 ± 0.37	62.06 ± 0.14
N	9.93 ± 0.28	9.7 ± 0.06	7.3	9.99 ± 0.3	9.51 ± 0.58	-
Mn	2.85 ± 0.08	3.76 ± 0.27	5.2	2.62 ± 0.02	3.51 ± 0.07	6.76 ± 0.39
O	11.54 ± 0.08	11.5 ± 0.01	13.1	11.7 ± 0.06	11.41 ± 0.16	18.04 ± 0.11
Rh	-	-	-	0.78 ± 0.03	1.17 ± 0.07	6.42 ± 0.08
Cl	0.1 ± 0	0.1 ± 0.01	0.2	0.3 ± 0.01	0.43 ± 0.01	0.65 ± 0.04
Na	0.11 ± 0.06	-	0.1	0.13 ± 0.08	0.08 ± 0.01	1.63 ± 0.29
F	-	-	-	1.72 ± 0.08	0.35 ± 0.09	2.15 ± 0.41
B	0.12 ± 0.06	-	0.4	0.37 ± 0.04	0.41 ± 0.06	2.31 ± 0.23
Si	0.39 ± 0	0.24 ± 0.04	0.6	-	-	-
S	0.16 ± 0.01	-	-	0.32 ± 0.08	-	-

Table S3: Atomic% data for **1**-used normalization to remove excess of SiO_2 contaminant as presented in Table S2. [a] Estimated value for Si based sample **1**.

Elements	**1** used	**1** used (Excluding excess of SiO_2)	**1** used (Normalized)
C	45.78 ± 0.47	45	73.0
N	4.54 ± 0.33	4.5	7.3
Mn	3.18 ± 0.01	3.18	5.2
O	33.22 ± 0.11	8.1	13.1
Rh	-	-	-
Cl	0.14 ± 0.01	0.14	0.2
Na	0.04 ± 0.02	0.04	0.1
F	-	-	-
B	0.27 ± 0.14	0.27	0.4
Si	12.85 ± 0.12	0.4[a]	0.6
S	-	-	-
total	98.98	61.63	100.0

B.8 High resolution spectra

Rh 3d

Fitting of the Rh 3d peak was undertaken using a combination of components based on lineshapes LA(1.2,3,2) for Rh^0 (red), LF(1,1,10,200) for doublet 2 (blue) and LF(0.9,1.1,10,200) for doublet 3 (green). A peak separation of 4.7 eV was used for each doublet.

Table S4: Rh $3d_{5/2}$ peak positions based on fitting presented in Figure 10 and tentative peak assignments based on literature values.

Sample	Peak position (eV) and tentative assignment for Rh $3d_{5/2}$					
	Doublet 1 (red)		Doublet 2 (blue)		Doublet 3 (green)	
1-Rh-BF4	307.0	Rh^{0} [2]	308.6	Rh(I)^	310.1	Rh(III)&
1-Rh-BF4-5%H2	307.5	Rh^0	308.4	Rh(I)^ and Rh_2O_3 #	310.1	Rh(III)&
1-Rh-BF4-used	307.5	Rh^0	308.4	Rh_2O_3 #	309.8	Rh(III)&

^Rh(I) has binding energy values in the literature at 308.3 eV[3] and 309 eV[4] for $Rh_2(CO)_4Cl_2$ and 308.5 eV and 308.3 eV for (acrylic resin)-NC-Rh(PPh$_3$)$_2$Cl and (acrylic resin)-NC-Rh, respectively[5]. &Rh(III) from oxidised Rh bound to linker has binding energy values in the range of 309.3 – 310.4 eV[2]. #Rh(III) as Rh_2O_3 has reported BE of 308.3 eV [6] and 308.4 eV[3].

N 1s

High resolution N 1s spectra of the ligand (H_2L) component of the MOF was collected to assist with the nitrogen peak assignment. The ligand H_2L is prepared via a 2 step synthesis, starting from bis(3,5-dimethylpyrazol-1-yl)methane, iodination to give (bis(3,5-dimethyl-4-iodopyrazol-1-yl)methane) and Suzuki coupling to give the ligand (H_2L). These 3 compounds were examined and for the first two compounds, a pair of peaks are observed in the N 1s spectra at approximately 398.8 eV (imine) and 400.4 eV (amine) with an intensity ratio (N2:N3) of 45:55. For the third step, where a pair of benzene rings with an acid group on either end are added and represents the ligand used in 1, both peaks are shifted to higher binding energy (399.2 eV and 400.7 eV) (Figure S11).

For the parent samples **1** and **1·Rh-BF4**, the high-resolution N 1s spectra could be fit with two components at approximately 399.5 eV and 401.1 eV (Figure 11), representing a further shift to higher binding energy compared to the ligand spectra (Figure S11c). Upshifting of N components upon coordination has been observed previously, for example for Pd and Mn coordination of bipyridine.[7] However it is noted that the binding energy shift seen here is significant compared to the original di-pyrazole spectrum, where organic N components in the range of 401 to 402 eV would generally be associated with N+, such as quaternary amine.[8] For **1·Rh-BF$_4$** and **1·Rh-BF$_4$-5%H$_2$**, the samples presented a shoulder on the lower binding energy side of the spectra (~ 397.8 eV) representing a small contribution consistent with nitride. Interestingly, using the original ligand (H$_2$L) N 1s spectrum as a model fit component, the N 1s for both parent samples can be fit using 2 components with a ratio of approximately 1:1. The peak position of the lower binding energy component (MC1) is consistent with the original ligand spectrum, while the other component (MC2) is shifted by approximately +0.7 eV. Based on this fit, the higher binding energy contribution would represent the ligand coordinated with the Mn, while the lower binding energy contribution would represent the ligand flanked by two Mn nodes in the MOF structure. Considering this hypothesis, the ratio between the two components MC1:MC2 should be 1:2, instead of 1:1. We believe that this difference is due to either surface orientation or a different stoichiometry on the surface of the MOF comparing to the interior. It is worth noting that after heat treatment, the ratio between MC1:MC2 moves closer to the expected 0.5. For 1·Rh-BF$_4$-5%H$_2$ it is 43/57 or 0.75, For 1-5%H$_2$, the ratio is 33%/67% or 0.49, approximately the expected value. Therefore, it is likely that the discrepancy observed for the parent samples is due, at least in part, to the presence of N-based contamination, likely organic.
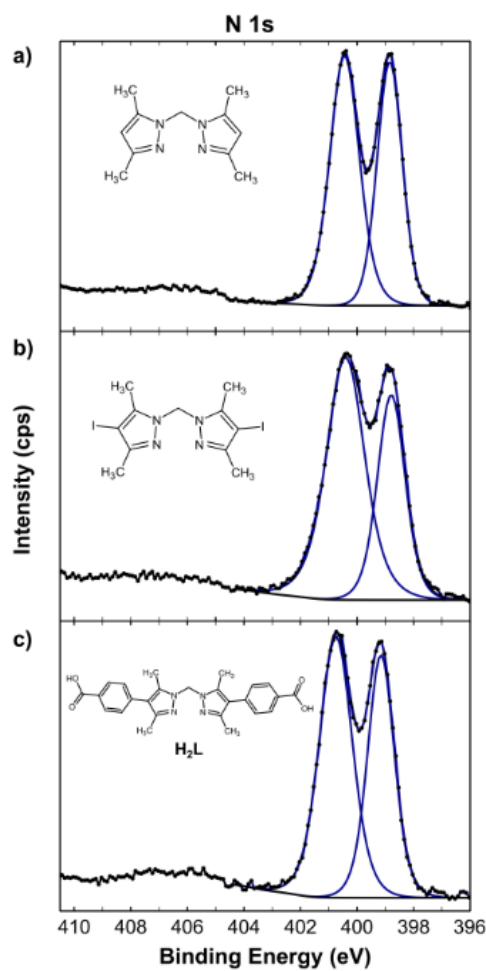
Figure S13: Selected, representative high resolution N 1s spectra of Bis(3,5-dimethylpyrazol-1-yl)methane (a), bis(3,5-dimethyl-4-iodo-1H-pyrazol-1-yl)methane (b), and H_2L (c).

Table S5: Results from peak fitting of Mn 2p spectra for each fitting component MnX where X is 1 to 7. The relative fraction of intensity for the satellite peak (component Mn7) for each sample w.r.t. 1.

Pos. (eV)	1	1-5%H2	1-used	1-Rh-BF4	1-Rh-BF4-5%H2)	1-Rh-BF4-used
Mn1	639.1	639.2	639.7	638.7	639.4	639.3
Mn2	640.6	640.6	640.5	640.6	640.7	640.7
Mn3	641.5	641.4	641.3	641.4	641.6	641.5
Mn4	642.4	642.3	642.2	642.2	642.5	642.5
Mn5	643.2	643.1	643.2	643.2	643.4	643.3
Mn6	644.2	644.0	644.2	644.5	644.4	644.2
Mn7	646.1	646.1	645.8	646.3	646.2	646.4
Relative fraction of Mn, %						
Mn1	2.7	1.5	8.6	0.7	2.5	1.5
Mn2	25.5	22.7	17.4	25.1	23.7	14.5
Mn3	23.3	20.6	27.8	20.9	23.4	26.8
Mn4	18.0	17.8	22.5	19.6	19.0	24.5
Mn5	9.2	14.2	11.9	13.4	10.3	12.4
Mn6	4.3	5.6	5.3	4.2	3.4	8.9
Mn7	17.1	17.7	6.6	16.1	17.7	11.4
Relative fraction (w.r.t. "1" or "1-Rh-BF4")						
Mn7	1.00	1.04	0.39	1.00	1.10	0.71

C. References

[1]   a) W. M. Bloch, A. Burgun, C. J. Coghlan, R. Lee, M. L. Coote, C. J. Doonan, et al. Capturing snapshots of post-synthetic metallation chemistry in metal–organic frameworks. Nat Chem. **2014**, *6*, 906; b) A. Burgun, C. J. Coghlan, D. M. Huang, W. Chen, S. Horike, S. Kitagawa, et al. Mapping-Out Catalytic Processes in a Metal–Organic Framework with Single-Crystal X-ray Crystallography. Angew Chem Int Ed. **2017**, *56*, 8412.

[2]   N. F. Goldshleger, B. I. Azbel, Y. I. Isakov, E. S. Shpiro, K. M. Minachev. Selective rhodium-containing zeolite catalysts for cyclodimerization of bicyclo 2.2.1 hepta-2,5-diene. J Mol Catal A: Chem. **1996**, *106*, 159.

[3]   Y. Okamoto, N. Ishida, T. Imanaka, S. Teranishi. Active States of Rhodium in Rhodium Exchanged Y Zeolite Catalysts for Hydrogenation of Ethylene and Acetylene and Dimerization of Ethylene Studied with X-Ray Photoelectron Spectroscopy. J Catal. **1979**, *58*, 82.

[4]   NIST X-ray Photoelectron Spectroscopy Database, NIST Standard Reference Database Number 20, National Institute of Standards and Technology, Gaithersburg MD, 20899, **2000**, DOI: 10.18434/T4T88K (retrieved 2015).

[5]   R. Giannandrea, P. Mastrorilli, G. Zaccaria, C. F. Nobile. Hydrogenation of organic substrates by isocyanide polymer-bound Rh(PPh(3))(3)Cl. J Mol Catal A: Chem. **1996**, *109*, 113.

[6]   Y. Abe, K. Kato, M. Kawamura, K. Sasaki. Rhodium and Rhodium Oxide Thin Films Characterized by XPS. Surface Science Spectra. **2001**, *8*, 117.

[7]   W. Leng, R. Ge, B. Dong, C. Wang, Y. Gao. Bimetallic docked covalent organic frameworks with high catalytic performance towards tandem reactions. RSC Adv. **2016**, *6*, 37403.

[8]   a) G. Beamson, D. Briggs. *High Resolution XPS of Organic Polymers: The Scienta ESCA300 Database* **1992** (Wiley); b) C. D. Easton, A. J. Bullock, G. Gigliobianco, S. L. McArthur, S. MacNeil. Application of layer-by-layer coatings to tissue scaffolds - development of an angiogenic biomaterial. J Mater Chem B. **2014**, *2*, 5558.